Chapter 3

Physical and electrochemical characterization of conducting polymer-based nanocomposites

This chapter explained the physical and electrochemical properties of PEDOT-PSS and PANI based nanocomposites. A systematic study of structural, morphological and vibrational properties of the synthesized conducting polymers and their nanocomposites were carried out through XRD, FESEM, FTIR respectively. An investigation on the electrocatalytic behaviour and charge transfer kinetics of the prepared electrodes has been performed by employing cyclic voltammetry and electrochemical impedance spectroscopy.

3.1. XRD analysis

XRD is carried out to study the structural property of the electrochemically synthesized PEDOT-PSS and chemically synthesized PANI and their nanocomposites. At first, the XRD spectra of PEDOT-PSS/ITO and its composites GO/PEDOT-PSS/ITO and AuNP/GO/PEDOT-PSS/ITO is discussed. Secondly, the structural property of PEDOT-PSS/ITO and its composites WS_2/PEDOT-PSS/ITO and AuNP/WS_2/PEDOT-PSS/ITO is explained. Third subsection discusses the XRD analysis of PANI and PANI-PVA nanofibers prepared by electrospinning.

3.1.1. AuNP/GO/PEDOT-PSS

The XRD patterns of synthesized PEDOT-PSS, GO/PEDOT-PSS and AuNP/GO/PEDOT-PSS/ITO electrode in the Bragg's angle region of 10 to 80^o is shown in Figure 3.1. The broad peak observed at 25^o for pristine PEDOT-PSS is attributed to (010) plane [1,2]. In GO/PEDOT-PSS electrode, the diffraction peak at 13.36° is the evidence of the characteristic peak (002) of GO [3]. In AuNP/GO/PEDOT-PSS, the high intense diffraction peak at 38.29^0 is attributed to (111) plane. AuNPs showed other peaks at 44.55^o, 64.87^o and 77.75^o which are ascribed to (200), (220) and (311); respectively [4,5]. Few intense diffraction peaks observed at 21.36◦, 30.33◦, 35.28◦, 41.46◦, 50.67◦, 60.21◦ corresponds to (211), (222), (400), (411), (440), and (622) which arises due to presence of ITO electrode [6]. Using Scherrer's equation, $d = k\lambda/\beta \cos\theta$, average crystallite size of the AuNPs for (111) plane was calculated to be 15.6 nm. In Scherrer equation, λ (1.54056 A^o) represents the wavelength of the source of x-rays, k represents Scherrer constant which ranges from 0.9 to 1 (here we have taken 0.9), β corresponds to the full width at half maxima (FWHM) for the (111) diffraction plane in radian and the Bragg angle is represented by θ in degrees [7,1].

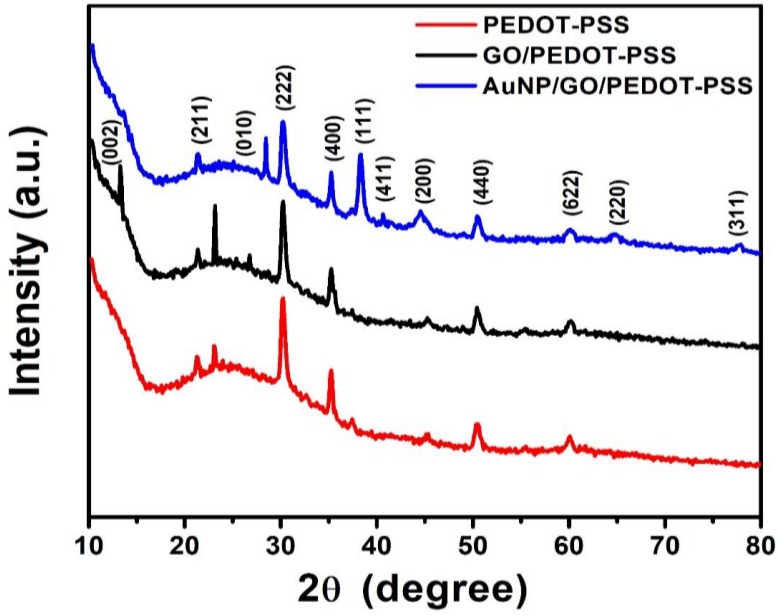

Figure 3.1: XRD spectra of PEDOT-PSS, GO/PEDOT-PSS and AuNP/GO/PEDOT-PSS films over ITO electrode.

3.1.2. AuNP/WS_2/PEDOT-PSS

XRD spectra of prepared PEDOT-PSS, WS_2/PEDOT-PSS and AuNP/WS_2/PEDOT-PSS are displayed in Figure 3.2.

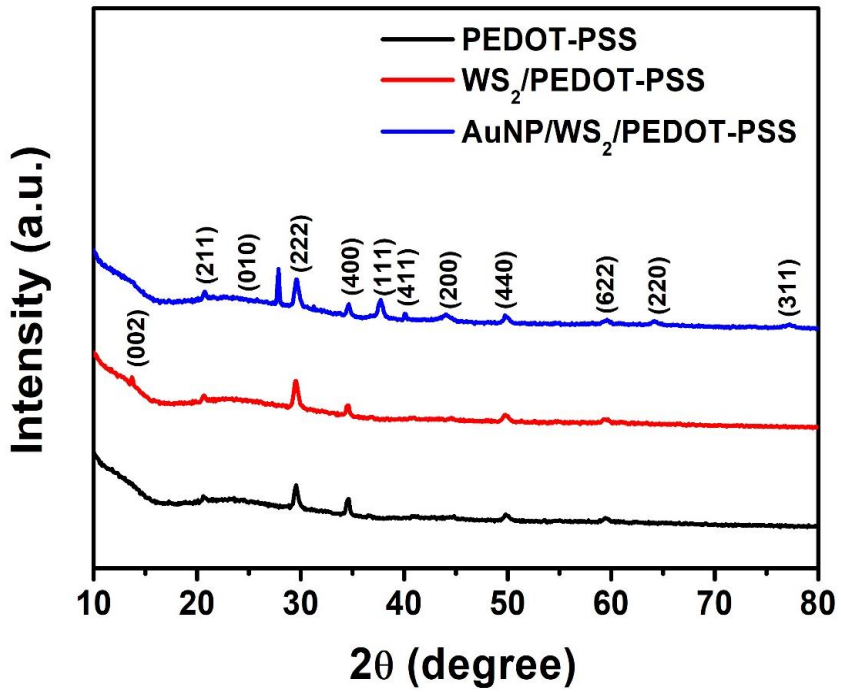

Figure 3.2: XRD spectra of PEDOT-PSS, WS_2/PEDOT-PSS and AuNP/WS_2/PEDOT-PSS films over ITO electrode.

Pure PEDOT-PSS exhibited its characteristic broad peak around 25^0 corresponding to (010) plane [1,2]. In the WS_2 modified PEDOT-PSS/ITO electrode, the peak around 13.64^0 gives the evidence of presence of WS_2 with (h,k,l) value (002) [8-11]. In the ternary composite system, AuNP showed its strong diffraction peak around 38.29° corresponding to the (111) plane. Other peaks located at 44.15°, 64.34°, 77.22° are assigned to (200), (220) and (311) planes of AuNP [4,5]. Using Scherrer equation [7], the average size of the AuNP for the (111) was calculated and found to be 18.7 nm. Presence of ITO electrode resulted appearance of few diffraction peaks at 20.63°, 29.65°, 34.59°, 49.84°, 59.61° corresponding to (211), (222), (400), (440) and (622) planes respectively [6].

3.1.3. PANI-PVA

The XRD patterns of the synthesized PANI and PANI/PVA are presented in Figure 3.3. Pure PANI displayed diffraction peaks at $2\Theta = 14.7^0$, 17.67^0 and 23.6^0 denoting h, k, l values (011), (020) and (200) respectively [12-14]. These specific peaks identify the repetition unit of the PANI molecule's chain and its periodicity with respect to the backbone chain of the polymer which originates in the crystalline portions of an amorphous form. PANI/PVA composite depicted a single characteristic peak at $2\Theta = 19.7^0$, which occurred due to the diffraction of PVA denoting h, k, l value (100). In the matrix of PVA, PANI peak overlaps PVA peak, indicating excellent reinforcing properties of PANI [15].

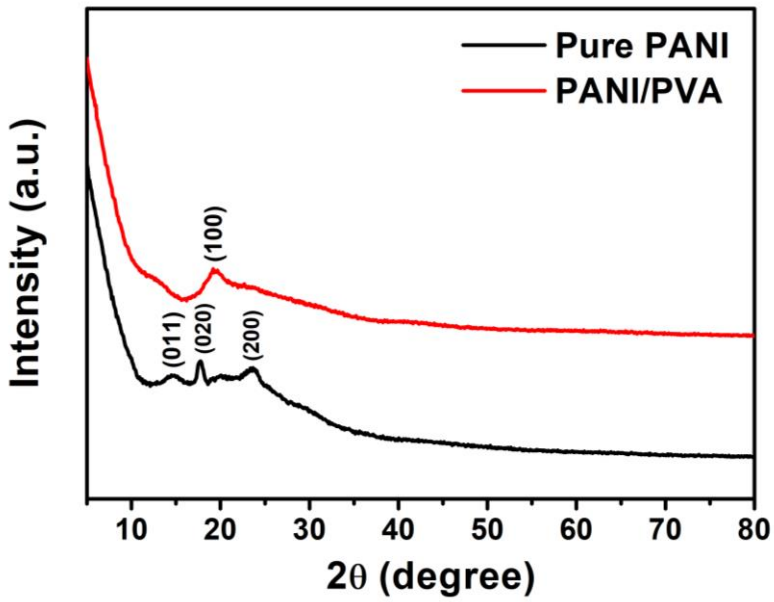

Figure 3.3: XRD plot of pure PANI, PANI/PVA composite fibers.

3.2. FTIR analysis

FT-IR was carried out for the identification of various functional groups and vibrational modes of chemical bonds present within the synthesized PEDOT-PSS and PANI and its respective nanocomposites. First section deals with the FTIR analysis of PEDOT-PSS/ITO and its composites GO/PEDOT-PSS/ITO and AuNP/GO/PEDOT-PSS/ITO. Secondly, the vibrational property of PEDOT-PSS/ITO and its composites WS_2/PEDOT-PSS/ITO and AuNP/WS_2/PEDOT-PSS/ITO are discussed. Third subsection explains the FTIR analysis of PANI and PANI-PVA nanofibers prepared by electrospinning.

3.2.1. AuNP/GO/PEDOT-PSS

In PEDOT-PSS, the peaks at 2920 cm^{-1} and 2856 cm^{-1} corresponds to asymmetric and symmetric stretching of CH_2 respectively, Figure 3.4 [16]. The significant peak at 1638 cm^{-1} corresponds to symmetric C=C stretching. The peaks located around 1331 cm^{-1} and 1461 cm^{-1} are due to the stretching of C–C and C=C of the quinoidal structure, which originates from the thiophene ring respectively [17]. The peak located at 1080 cm^{-1} corresponds to the symmetric stretching of S=O present in SO_3^- group of PSS. A band around 970 cm^{-1} is observed due to the deformation in ethylene dioxy ring. while the peak observed at 635 cm^{-1} and 828 cm^{-1} corresponds to C-S stretching of thiophene ring and S-O linkage of PSS, respectively [18].

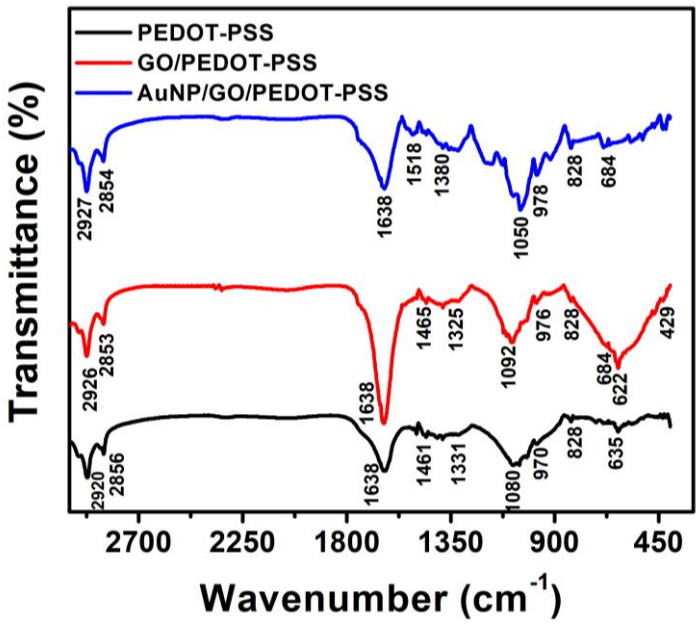

Figure 3.4: FTIR spectra of PEDOT-PSS, GO/PEDOT-PSS and AuNP/GO/PEDOT-PSS films over ITO electrode.

In the binary system GO/PEDOT-PSS, the evidence of several types of functional groups that are generated by oxidation are confirmed by FTIR spectra. The vibration modes appeared between the range 2800–3000 cm^{-1} are due to the C–H stretching mode [19]. In PEDOT-PSS-GO composite system the vibrational peak located at 1638 cm^{-1} is attributed to aromatic C=C bending [20,21]. The shifted peaks at 1325 cm^{-1} is attributed to the vibrational modes of epoxide (C–O–C). The peaks that appeared in the range of 600–700 cm^{-1} can be attributed to the C–H deformation in the polymer-GO composite. Due to C=C out of plane benzene ring bending of GO sheets, an absorption peak at 429 cm^{-1} is observed [22].

In the ternary hybrid system, the peak intensity decreased due to the deposition of AuNP over the polymer matrix. Shifting and disappearance of some less prominent peaks were also observed in the ternary system.

3.2.2. AuNP/WS_2/PEDOT-PSS

The FTIR spectra of all the synthesized electrodes: PEDOT-PSS, WS_2 incorporated PEDOT-PSS and AuNPs decorated WS_2/PEDOT-PSS are presented in Figure 3.5. As discussed above, in PEDOT-PSS electrodes, the vibrational peak at ~1638 cm^{-1} corresponds to stretching of the C=C alkane [16,23]. The peak locations of ~2924 cm^{-1} and 2855 cm^{-1} are caused by the asymmetric stretching of the CH_2 molecules as well as the symmetric vibrations [17,16]. The peak position at ~1078 cm^{-1} corresponds to the symmetric stretching of the S=O which is present in the SO_3^- group of PSS. A vibrational band at ~1332 cm^{-1} corresponded to the C=C stretching at the quinoidal structure of the thiophene ring, whereas C-C stretching is responsible for another vibration band appearing at ~1488 cm^{-1} [23-25]. A peak position at ~630 cm^{-1} is tied to C-S stretching within the thiophene ring, and another vibrational peak at ~832 cm^{-1} is related to the S-O linkages of the PSS [18]. On the other hand, the band located at ~980 cm^{-1} can be attributed to the deformation occurring within the ethylene dioxy ring [23,25].

In the binary electrode, W-S bonds are assigned to the peak positions at ~560 cm^{-1} and 678 cm^{-1} in the WS_2/PEDOT-PSS system [26]. As consequence of the S-S bond, another peak has been observed at ~920 cm^{-1} [26-28]. To be mentioned, a suppression of vibrational bands was observed in the AuNPs decorated in the WS_2/PEDOT-PSS systems. This could be attributed to multiple layers of AuNPs deposited on the polymeric composite electrodes, potentially creating constraints that limit the stretching of molecular bonds.

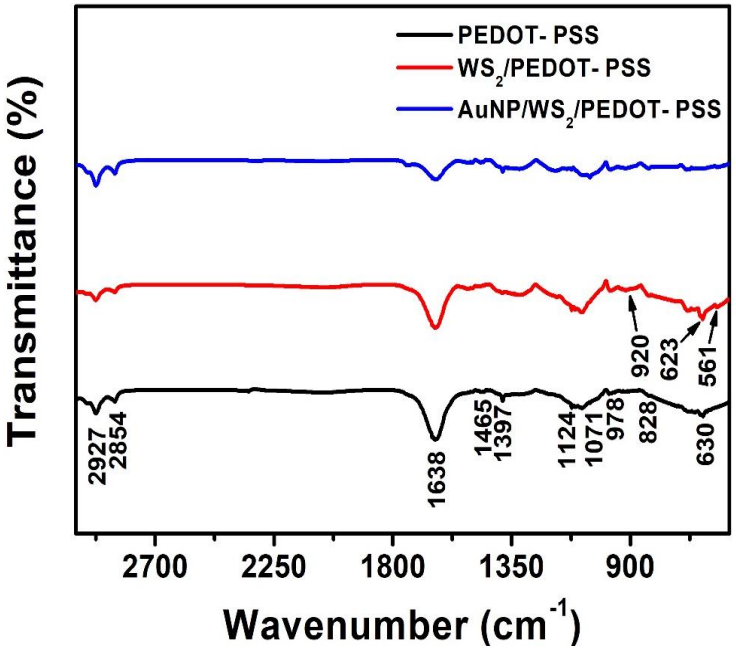

Figure 3.5: FTIR spectra of synthesized PEDOT-PSS, WS_2/PEDOT-PSS, and AuNP/WS_2/PEDOT-PSS films.

3.2.3. PANI-PVA

FTIR spectra of synthesized PANI and PANI/PVA nanofiber is shown in Figure 3.6. Pure PANI nanofibers shows characteristics peaks at 1584 cm^{-1} and 1491 cm^{-1} are attributed to the C=C stretching of quinoid ring and benzenoid ring respectively [29]. The peak position at 1297 cm^{-1} is assigned to the C-N stretching vibration of aromatic ring [30]. The vibrational peaks at 1148 cm^{-1} and 826 cm^{-1} corresponds to the in-plane bending and out-plane-bending of C-H, respectively [29].

In the PANI-PVA composite nanofiber system, the peak observed at 3400 cm^{-1} is attributed to N-H group of PANI and O-H group of PVA [31-33]. The peak located at 2926 cm^{-1} is due to the stretching vibration of aliphatic C-H group of PVA and aromatic C-H group of PANI [31,32,34]. The peak at 1446 cm^{-1} is arising due to plane deformation of C-H and O-H group of PVA. The characteristic peaks at 1328 cm^{-1} and 1097 cm^{-1} are due to the stretching vibration of -CH_2 group and C-O group in PVA, respectively [34]. In the composite system shifting in the peak position is found compared to the pristine PANI nanofiber system.

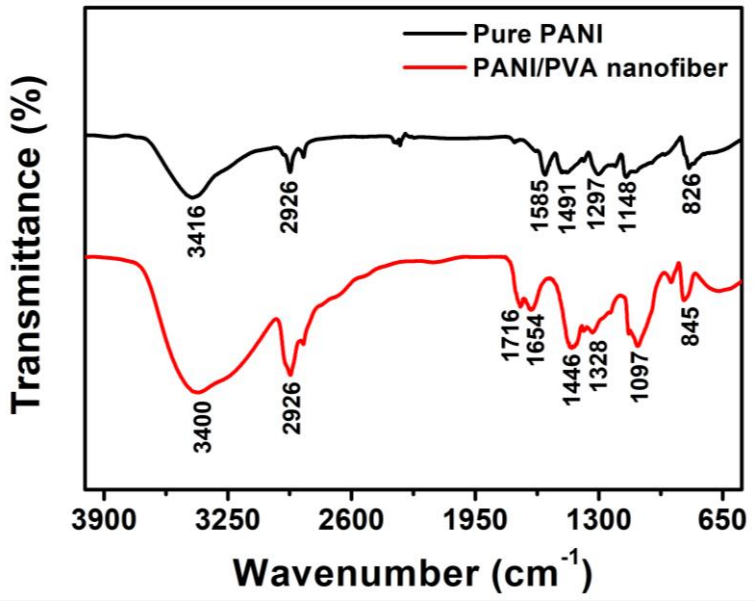

Figure 3.6: FTIR analysis of pure PANI, PANI/PVA composite fibers.

3.3. Morphological studies

FESEM was carried out to gain the information about surface morphology of the synthesized PEDOT-PSS and PANI and their nanocomposites. Again, to identify the elemental composition of all the synthesized materials EDX was adopted. First section illustrates the morphology and elemental composition of PEDOT-PSS/ITO, GO/PEDOT-PSS/ITO and AuNP/GO/PEDOT-PSS/ITO. Secondly, the FESEM micrograph and EDX analysis of PEDOT-PSS/ITO and its composites WS_2/PEDOT-PSS/ITO and AuNP/WS_2/PEDOT-PSS/ITO have been discussed. Third subsection explains the surface morphology of PANI and PANI-PVA nanofibers prepared by electrospinning.

3.3.1. AuNP/GO/PEDOT-PSS

The FESEM micrograph of synthesised PEDOT-PSS, GO/PEDOT-PSS and AuNP/GO/PEDOT-PSS is shown in Figure 3.7. PEDOT-PSS (Figure 3.7 (a)) shows porous microstructures with clusters (PEDOT) of size, ~200 nm to 900 nm. The clusters are found to be connected by PSS fibres, or chains. Incorporating GO on the polymer film in Figure 3.7 (c) results in the better dispersion of PEDOT and formation of smaller cluster of size 130 nm to 600 nm. It is assumed that the GO sheets are entrapped in between the polymer chains. Figure 3.7 (e) depicts the presence of 30-100 nm AuNPs over the polymer composite film with magnified view in Figure 3.7 (g,h). Further, disappearance of the fibrous structures has been observed after deposition of AuNPs over the GO/PEDOT-

PSS/ITO electrode surface suggesting incorporation of dense AuNPs in the composite electrode.

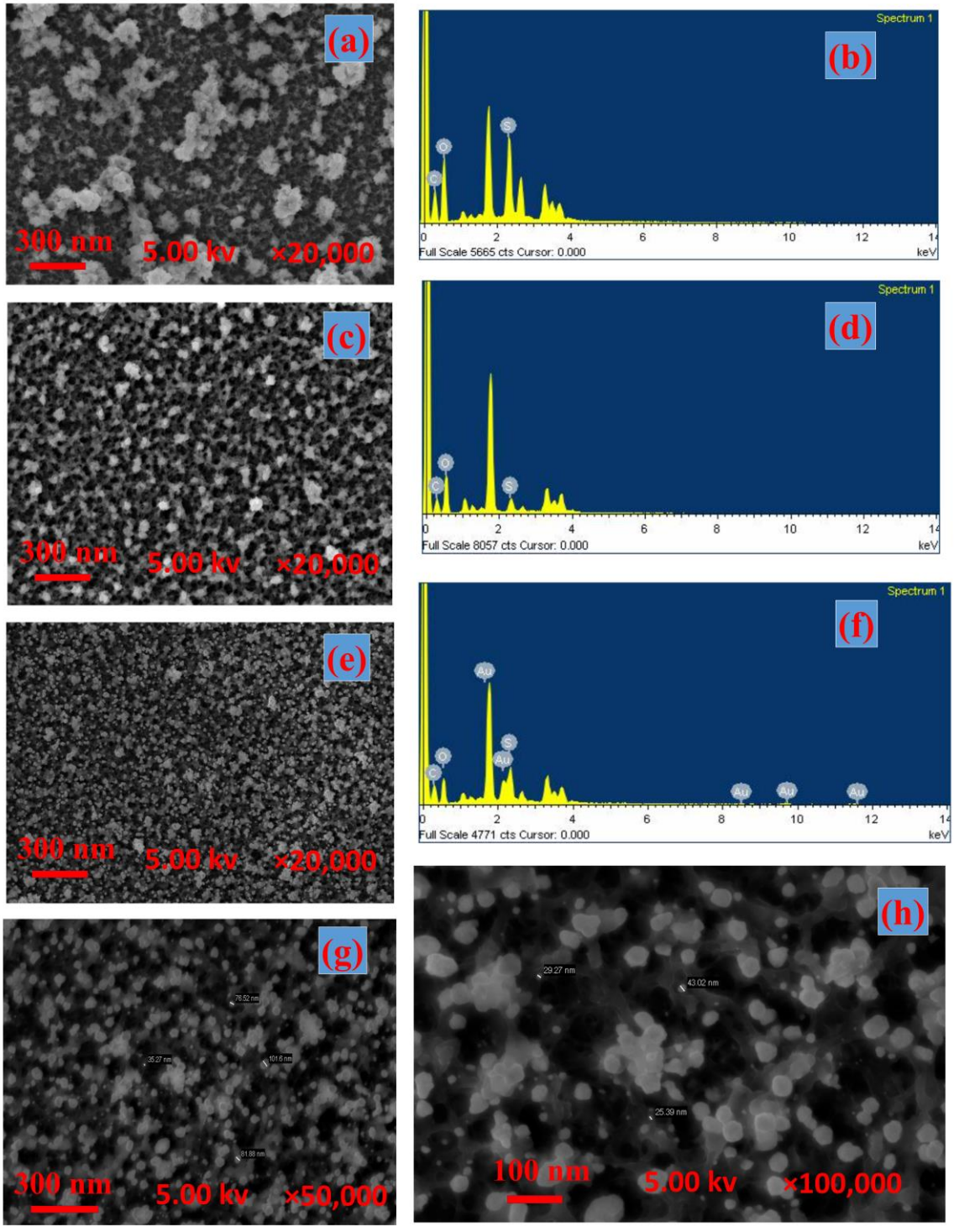

Figure 3.7: FESEM images of (a) PEDOT-PSS, (c) GO/PEDOT-PSS and (e) AuNP/GO/PEDOT-PSS films on ITO. (g,h) magnified view of Fig. (e). EDX analysis of (b) PEDOT-PSS, (d) GO/PEDOT-PSS and (f) AuNP/GO/PEDOT-PSS films on ITO.

To confirm the chemical compositions of the prepared films, EDX is performed for all the synthesized electrodes. The relative elemental percentage confirms the presence and concentration of different elements in the synthesized film. In Figure 3.7 (b), the X-ray emission spectra corresponding to the K-shell transition energy of carbon, oxygen and sulfur confirms the presence of these constituents in the PEDOT-PSS film. In case of GO/PEDOT-PSS, the relative atomic percentage of oxygen exceeds (Figure 3.7 (d)), which is due to the presence of the oxygen containing functional groups in the graphene oxide sheets. The deposition of gold nanoparticles over the GO/PEDOT-PSS film is confirmed by the emission spectra corresponding to M−shell transition energy of Au as seen in Figure 3.7 (f).

Elemental constituents of the synthesized electrodes obtained from EDX data

Table 3.1: Atomic percentage of the elemental constituents for; (a) PEDOT-PSS, (b) GO/PEDOT-PSS and (c) AuNP/GO/ PEDOT-PSS.

(a)

Element	Weight%	Atomic%
C K	38.25	47.71
O K	49.98	46.80
S K	11.77	5.50
Total	100.00	

(b)

Element	Weight%	Atomic%
C K	32.40	39.92
O K	62.32	57.64
S K	5.28	2.44
Total	100.00	

(c)

Element	Weight%	Atomic%
C K	36.70	53.46
O K	36.09	39.46
S K	10.21	5.57
Au M	17.00	1.51
Total	100.00	

3.3.2. AuNP/WS_2/PEDOT-PSS

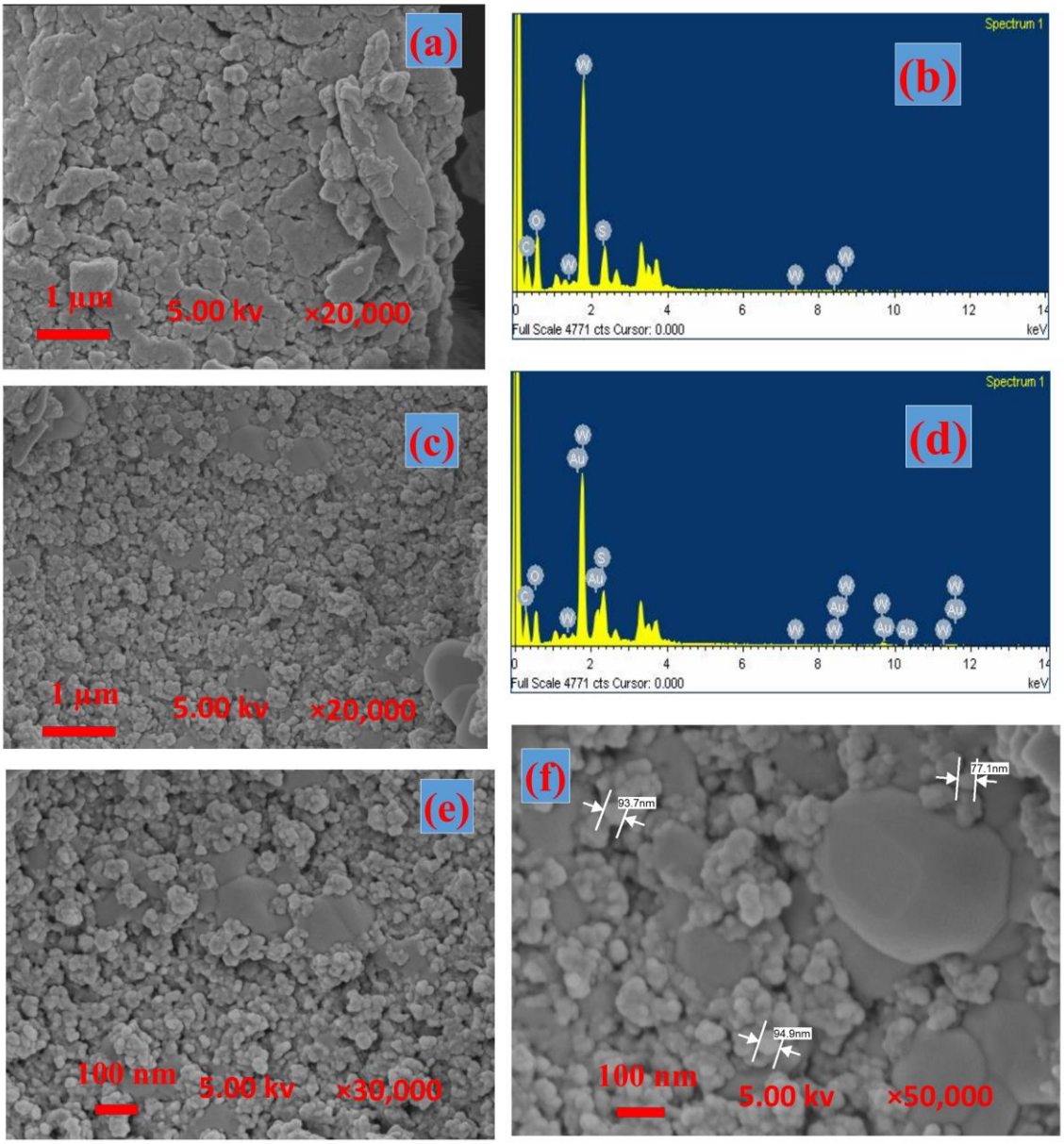

Figure 3.8: FESEM images of (a) WS_2/PEDOT-PSS and (c) AuNP/WS_2/PEDOT-PSS films on ITO. (e,f) magnified view of Fig. (c). EDX spectra of (b) WS_2/PEDOT-PSS and (d) AuNP/WS_2/PEDOT-PSS films on ITO.

FESEM micrographs of synthesized AuNP/WS_2/PEDOT-PSS/ITO and WS_2/PEDOT-PSS/ITO are displayed in Figure 3.8. WS_2/PEDOT-PSS displays formation of sheets like structures where WS_2 sheets are covered by polymer chain (Figure 3.8 (a)). After incorporation of Au over the surface of the WS_2/PEDOT-PSS system, Figure 3.8 (c) shows formation of spherical nanoparticles with a magnified view as shown in Figure 3.8 (e,f). But these metal particles faced agglomeration due to the multiple cycles of deposition over the surface of the WS_2/PEDOT-PSS film.

The EDX spectra of WS_2/PEDOT-PSS/ITO and AuNP/WS_2/PEDOT-PSS/ITO is shown in Figure 3.8 (b) and Figure 3.8 (d); respectively. Moreover, the energy dispersive X-ray spectra resulted in the presence of carbon, oxygen, sulfur, tungsten and gold leading to the formation of AuNPs decorated WS_2/PEDOT-PSS film. The elemental atomic percentage of each constituent can be found in Table 3.2.

Elemental constituents of the synthesized electrodes obtained from EDX data

Table 3.2: Atomic percentage of the elemental constituents for (a) WS_2/PEDOT-PSS and (b) AuNP/WS_2/PEDOT-PSS.

(a)

Element	Weight%	Atomic%
C K	28.39	45.04
O K	40.31	48.01
S K	7.55	4.49
W M	23.74	2.46
Total	100.00	

(b)

Element	Weight%	Atomic%
C K	34.40	57.49
O K	27.11	34.02
S K	8.47	5.30
W M	18.31	2.00
Au M	11.71	1.19
Total	100.00	

3.4.3. PANI-PVA

The FESEM micrograph of PANI particles covering the aluminium foil and PANI/PVA composite fibers is shown in Figure 3.9. Pristine PANI shows some micro to nano particles which got agglomerated and forms some clusters like structure (Figure 3.9 (a)). The clusters are connected by very less number of fibers and appeared highly porous. Formation of very less number of fibers might be due to the low viscosity of prepared

solution and solubility limitations of PANI in NMP. To improve the viscosity and processibility of PANI, one polymer namely PVA, is chosen as a binder. The morphology of PANI/PVA composite at different concentration of PVA is shown in Figure 3.9 (b-d).

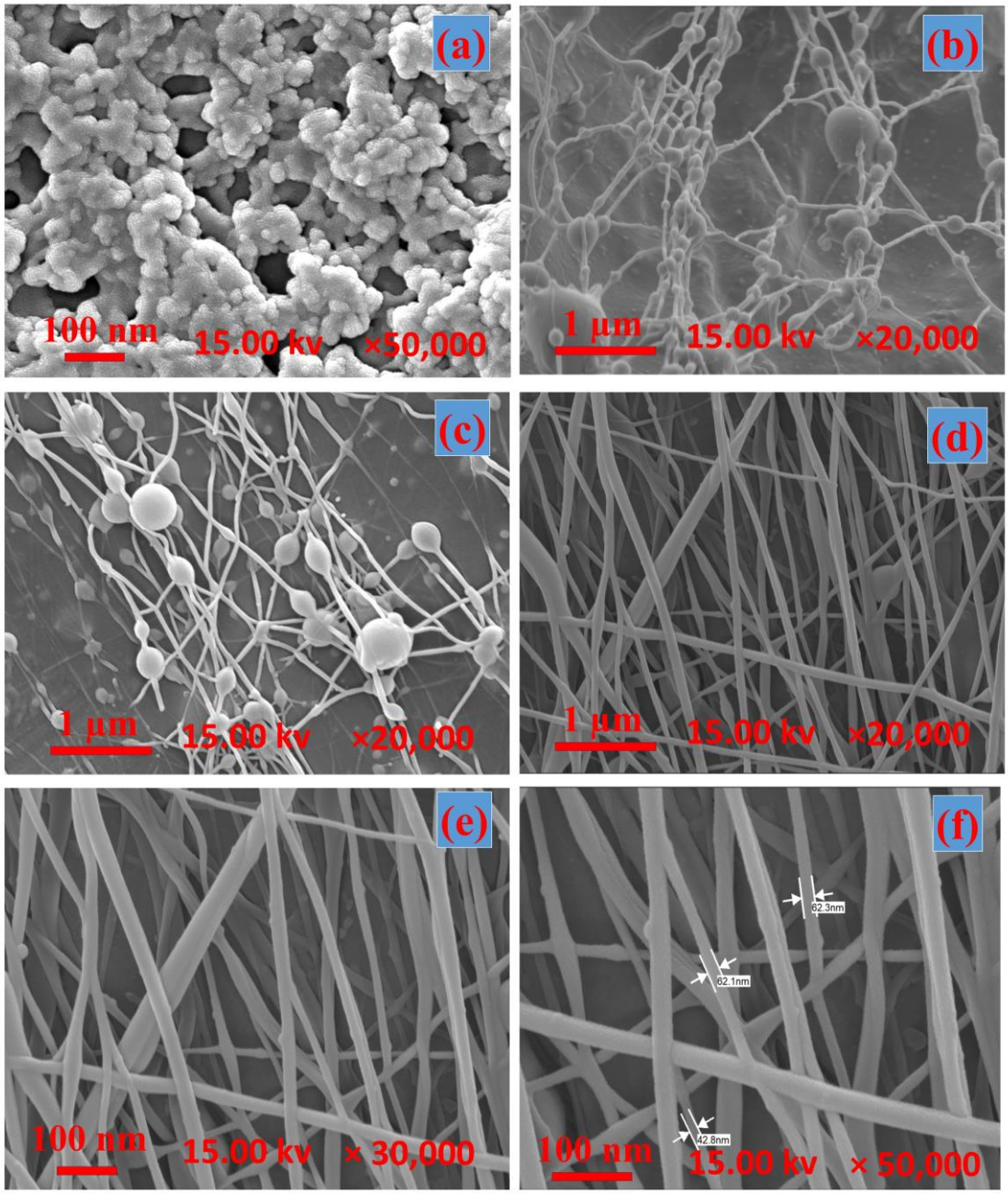

Figure 3.9: FESEM images of (a) PANI particles and PANI-PVA nanofibers (b) 1:1 ratio (c) 1:2 ratio (d) 1:3 ratio. (e,f) magnified view of (d).

PANI-PVA was optimized at different PVA ratio like 1:1 (Figure 3.9 (b)), 1:2 (Figure 3.9 (c)) and 1:3 (Figure 3.9 (d)) respectively. While the PVA content was less (Figure 3.9 (b,c)), formation of some beads can be found due to resistance of the jet to the extensional flow resulting from poor viscosity. However, after increasing the PVA content (PANI:PVA=1:3), Figure 3.9 (d) shows a large number of smooth fibers of diameter less than 100 nm with a magnified view as shown in Figure 3.9 (e,f).

3.4. Electrochemical properties of different PEDOT-PSS based composite electrodes

To understand the electrocatalytic activity and interfacial charge transfer kinetics, cyclic voltammetry (CV) and electrochemical impedance spectroscopy (EIS) were performed for all the prepared electrodes. CV and EIS were carried out for PEDOT-PSS, GO/PEDOT-PSS, WS_2/PEDOT-PSS, AuNP/GO/PEDOT-PSS and AuNP/WS_2/PEDOT-PSS electrodes at a scan rate of 20 mV/sec under potential window from -0.2 V to 1.2 V in 0.1 M phosphate buffer saline (PBS) as an electrolyte. Multifrequency impedance spectroscopy study was carried out for all the prepared electrodes with an ac signal of 10 mV within frequency range from 1 Hz to 1 MHz in PBS electrolyte.

3.4.1. Cyclic voltammetry analysis

Cyclic voltammetry curves of the synthesized PEDOT-PSS, GO/PEDOT-PSS, WS_2/PEDOT-PSS, AuNP/GO/PEDOT-PSS and AuNP anchored WS_2/PEDOT-PSS electrode is shown in Figure 3.10 (a). The CV curves (magnified view) for both the GO and WS_2 based system independently can be found in Figure 3.10 (b) and Figure 3.10 (c) respectively. To explore the electroactive properties of the prepared electrodes CV was performed for all the electrodes. The GO/PEDOT-PSS and WS_2/PEDOT-PSS systems showed the presence of no remarkable peaks. However, after electro-polymerization with GO, the area under the CV curve of the GO/PEDOT-PSS/ITO electrode increases with the deposition cycle. Similarly, area under the CV curves increases after electro polymerization of EDOT in presence of WS_2 and PSS due to higher conductivity and capacitance of the WS_2 and polymer composite system [35]. The area under the CV curve is related to the quantity of charge exchanged during the redox reaction. As the conductivity and capacitance increase in the composite electrode, it can affect the shape and size of the CV curve.

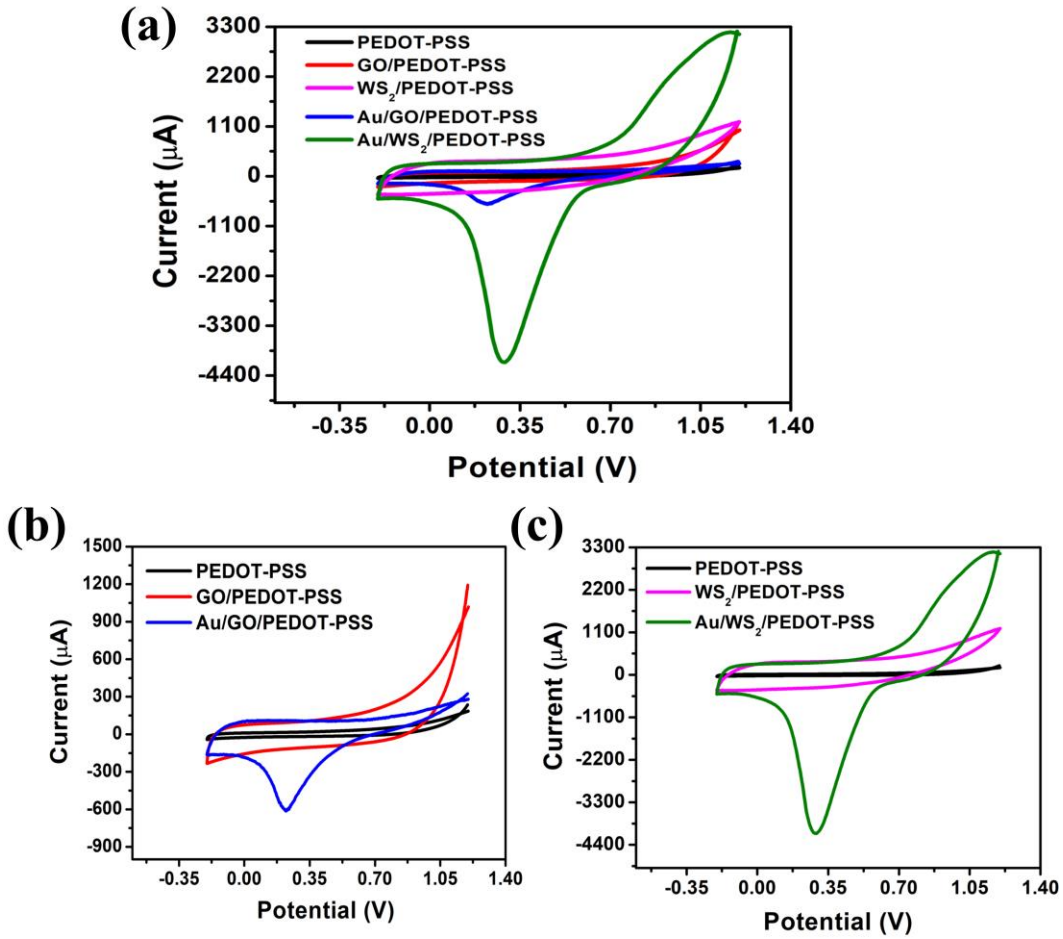

Figure 3.10: Cyclic voltammetry plot of (a) PEDOT-PSS, GO/PEDOT-PSS, WS_2/PEDOT-PSS, AuNP/GO/PEDOT-PSS and AuNP/WS_2/PEDOT-PSS films on ITO; (b) PEDOT-PSS/ITO, GO/PEDOT-PSS/ITO, Au/GO/PEDOT-PSS/ITO (c) PEDOT -PSS, WS_2/PEDOT-PSS and Au/WS_2/PEDOT-PSS/ITO.

Specifically, an increase in conductivity facilitates faster electron transfer between the electrode and the electrolyte species and leads to higher current response. While an increasing capacitance suggests more charge can be stored at the electrode-electrolyte interface. This allows for greater charge accumulation and redistribution during the CV scan, leading to a larger area under the curve. In AuNPs embedded GO/PEDOT-PSS/ITO ternary electrode (Figure 3.10 (b)), one reduction peak is clearly seen at 0.22 V owing to the reduction of Au. For Au/WS_2/PEDOT-PSS/ITO electrode (Figure 3.10 (c)), one reduction peak is observed at 0.28 V for reduction of gold from Au (3+) → Au (0) state [36, 37].

3.4.2. Electrochemical impedance spectroscopy

The electron transfer kinetics between the synthesized electrodes and electrolyte interface were characterized by EIS. EIS was performed with a small ac signal of 10 mV in the frequency range from 1 mHz to 1 MHz for PEDOT: PSS, GO/PEDOT-PSS, AuNP/GO/PEDOT-PSS, WS_2/PEDOT-PSS, AuNP/WS_2/PEDOT-PSS films on ITO electrode in PBS solution. The impedance spectra for the electrochemical cells with modified electrodes such as PEDOT-PSS, GO/PEDOT-PSS and AuNPs/GO/PEDOT-PSS respectively can be found in Figure 3.11 (a). Typical EIS spectra of synthesized WS_2/PEDOT-PSS and AuNP/WS_2/PEDOT-PSS electrodes over ITO are depicted in Figure 3.11 (b). The solid lines represent the impedance data while the dotted lines represent the fitted data. In the Nyquist plot, charge transfer resistance R_{ct} is represented by the diameter of the suppressed semicircle at higher frequencies followed by the diffusive part at low frequency region. Impedance data were fitted with an equivalent circuit shown in inset of both the plots. Equivalent circuit parameters consist of series resistance (R_1), charge transfer resistance (R_{ct}), double layer capacitor (C_2 or constant phase element Q_2), Warburg impedance (W_3) with another capacitor (C_3 or constant phase element Q_3). The fitted equivalent circuit for the PEDOT-PSS, GO/PEDOT-PSS and AuNPs/GO/PEDOT-PSS electrodes can be found in the inset of Figure 3.11 (a) where R_1 in series with the parallel combination of R_{ct} and C_2 and another parallel combination of W_3 which represents the diffusion in the polymer chain with C_3 representing the space charge layer amidst PEDOT and PSS rich grains.

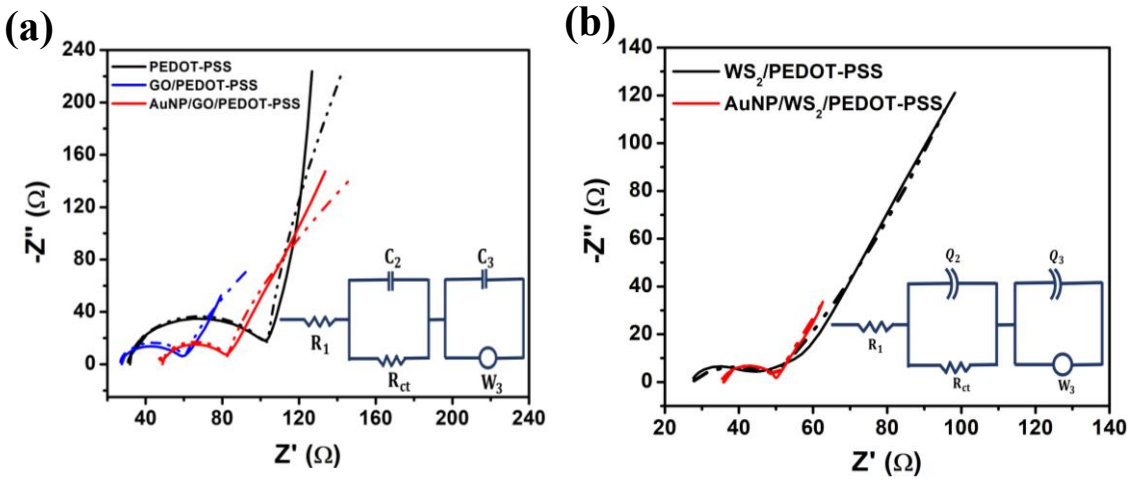

Figure 3.11: Nyquist plot of (a) PEDOT-PSS, GO/PEDOT-PSS, AuNP/GO/PEDOT-PSS (b) WS_2/PEDOT-PSS, AuNP/WS_2/PEDOT-PSS films on ITO.

Volkov et al. [38] reports that the major contribution to the capacitance of the two-phase PEDOT-PSS originates from electrical double layers formed along the interfaces between nanoscaled PEDOT rich and PSS-rich interconnected grains that comprises two phases of the bulk of PEDOT-PSS. The diffusive part comes into action due to the porous/interconnected nature of the conducting polymer film. The diffusive nature diminishes after incorporation of GO and AuNPs in the polymer film. This is confirmed from the significant decrease in the Warburg impedance (W_3) of the modified electrode after incorporation of GO and AuNP. The fitted parameter values of the equivalent circuit corresponding to all three electrodes namely; PEDOT-PSS/ITO, GO/PEDOT-PSS/ITO, AuNP/GO/PEDOT-PSS/ITO are shown in Table 3.3. The series resistance does not change much for all three electrodes. It is observed from the Table 3.3 that the charge transfer resistance (R_{ct}) value of PEDOT-PSS/ITO is 71.44 Ω which is slightly higher as compared to that of the other two electrode compositions. Simultaneously, PEDOT-PSS shows a maximum capacitance effect Q_2 (non-blocking electrode type) compared to other electrodes suggesting thinner space charge layer at the electrode/electrolyte interface.

The R_{ct} value of GO/PEDOT-PSS, AuNP/GO/PEDOT-PSS are 32.50 Ω and 28.79 Ω; respectively with slight decrease compared to PEDOT-PSS. The decrease in capacitance C_2 for GO and Au incorporation showed that by incorporating GO and Au, the cross-linked polymer structure forms continuous layer which helps in easier charge transfer between Au/GO and PEDOT-PSS but with a relatively a wider space charge layer/double layer at the electrode/electrolyte interface.

Table 3.3: EIS spectra fitted parameters of PEDOT-PSS/ITO, GO/PEDOT-PSS/ITO and AuNP/GO/PEDOT-PSS/ITO electrodes.

Serial number	Electrode	R_1 (Ω)	R_{ct} (Ω)	C_2 (μF)	C_3 (μF)	W_3 ($S.s^{1/2}$) ($x10^{-6}$)
1	PEDOT-PSS	31.82	71.44	7.386	564.4	2428
2	GO/PEDOT-PSS	27.61	32.50	3.660	370.4	1818
3	AuNP/GO/PEDOT-PSS	50.76	28.79	4.616	503.3	1490

The relatively low decrease observed in Q_3 for modified electrodes could be due to the increase in the space charge layer between the PEDOT-rich and PSS-rich interconnected grains with additions of GO and Au nanoparticles in between. The Nyquist plot for synthesized WS_2/PEDOT-PSS/ITO and AuNP/WS_2/PEDOT-PSS films is displayed in Figure 3.11 (b). The equivalent circuit used to fit the impedance data can be found in the inset of Figure 3.11 (b). The equivalent circuit parameters, R_1 is in series with the parallel combination of R_{ct} and Q_2 (constant phase element) and another parallel combination of W_3 with Q_3 (Constant phase element). Here, C_2 and C_3 are replaced by Q_2 and Q_3. To be mentioned, Q_2 is due to the formation of a double layer capacitor at the interface, Q_3 is the space charge layer modification between PEDOT and PSS rich grains in presence of WS_2 and Au. As mentioned earlier, W_3 represents the Warburg impedance originating due to diffusion inside the layered interconnected polymer structure. The value of fitted equivalent circuit parameters for the respective electrodes can be found in Table 3.4. The R_{ct} value of WS_2/PEDOT-PSS electrode is 22.45 Ω while it decreases to 13.43 Ω after electrodeposition of AuNPs over the surface of the WS_2/PEDOT-PSS electrode as a result of better charge transfer at the interface after incorporation of gold. Again, Q_2 value is found to be decreased after incorporation of Au in the WS_2 – polymer composite as a result of continuous conducting layers of gold which helps in easier charge transfer at the interface. Modification of the space charge layer between PEDOT and PSS rich grains with additional WS_2 and Au layers leads to a lowered value of Q_3 for the tertiary electrode.

Table 3.4: EIS spectra fitted parameters of WS_2/PEDOT-PSS/ITO and AuNP/WS_2/PEDOT-PSS/ITO electrodes.

Serial number	Electrode	R_1 (Ω)	R_{ct} (Ω)	Q_2 ($\times 10^{-6}$) $S.s^n$	Q_3 ($\times 10^{-3}$) $S.s^n$	W_3 ($\times 10^{-6}$) ($S.s^{1/2}$)
1	WS_2/PEDOT-PSS	27.53	22.45	235.7, n= 0.634 Q_2^n =31.92	10.28, n= 0.739 Q_3^n=5.59	903.5
2	AuNP/WS_2/PEDOT-PSS	35.88	13.43	6.63, n= 0.982 Q_2^n =6.40	6.607, n= 0.757 Q_3^n=4.17	32.20

3.4.3. Estimation of electroactive area

The geometric area of the ITO electrode used was 1 cm^2. To investigate and compare the electrochemical behaviour of all the modified ITO electrodes, the Randles-Sevcik equation was used to assess the electroactive area of all the synthesized electrode systems using $K_3[Fe(CN)_6]$ redox couple of 5 mM concentration. This equation essentially establishes a linear relationship between the anodic peak current (i_p)/cathodic peak current (i_c) and the square root of the scan rate ($\upsilon^{1/2}$), expressed as [23]:

$$i_p = 2.69 \times 10^5 \times n^{3/2} AD^{1/2} C\upsilon^{1/2} \quad (3.1)$$

In the equation 'n' represents the number of electrons transferred in the redox process, 'A' denotes electroactive area of the electrodes in cm^2, 'D' is the diffusion coefficient in cm^2 s^{-1} (~ 10^{-5} cm^2 /s) [35]. 'C' is the concentration of the redox active species present in the electrolyte in mol cm^{-3}. 'υ' is the scan rate in Vs^{-1}.

The value of A can be calculated from the slope (m) of the i_p vs $\upsilon^{1/2}$ plot,

$A = \frac{m}{2.69 \times 10^5 \times n^{3/2} D^{1/2} C}$, where m is the slope of the i_p vs $\upsilon^{1/2}$ plot.

Electroactive area estimated for various electrodes is given in Table 3.5. The CV responses of all the modified ITO electrodes namely PEDOT-PSS, GO/PEDOT-PSS, WS_2/PEDOT-PSS, AuNP/GO/PEDOT-PSS, AuNP/WS_2/PEDOT-PSS, PANI and PANI-PVA is illustrated in Figure 3.12 (a–f) respectively. CV were recorded by varying the scan rates from 5 to 40 mV/s within a potential window of −0.2 V to +0.8 V (vs. Ag/AgCl) in a PBS solution containing 5 mM of $K_3[Fe(CN)_6]$ as a redox agent. Subsequently the peak oxidation current (i_{pa}) is plotted against the square root of the scan rate ($\upsilon^{1/2}$) for the respective CV cycles, and performed a linear fitting of the resulting data points.

Table 3.5: Calculated values of electroactive area.

Electrode	Geometrical area (cm^2)	Electroactive area (cm^2)
PEDOT-PSS	1	0.0618
GO/PEDOT-PSS	1	0.1116
WS_2/PEDOT-PSS	1	0.1871
AuNP/GO/PEDOT-PSS	1	0.2805
AuNP/WS_2/PEDOT-PSS	1	0.3523
PANI-PVA	1	0.4238

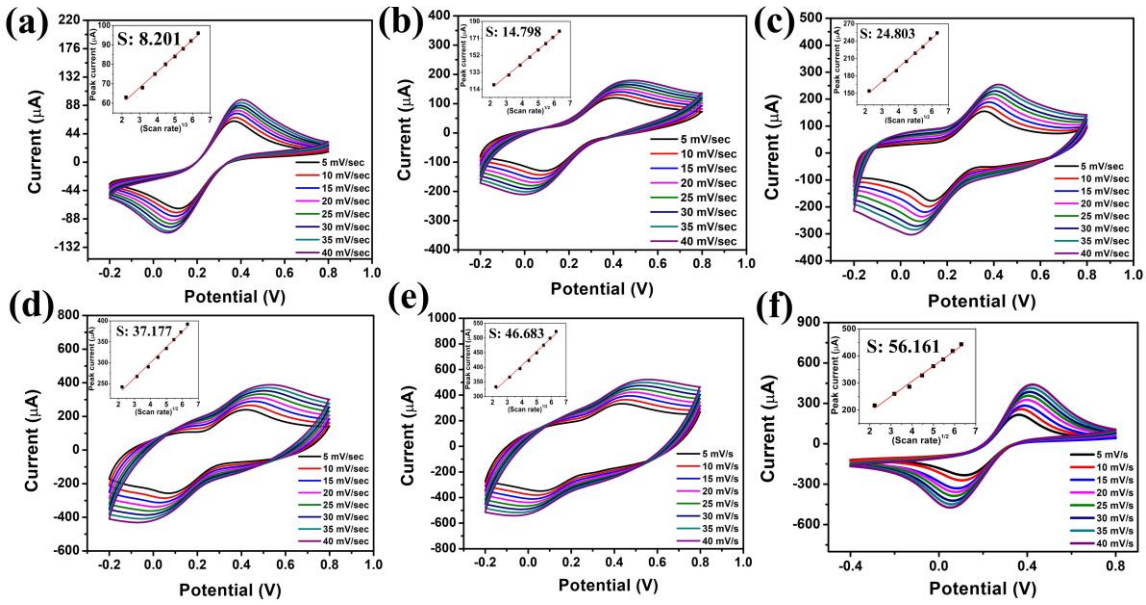

Figure 3.12: CV plots recorded with scan rate variation for ITO electrode modified with (a) PEDOT-PSS, (b) GO/PEDOT-PSS, (c) WS_2/PEDOT-PSS, (d) AuNP/GO/PEDOT-PSS, (e) AuNP/WS_2/PEDOT-PSS, (f) PANI-PVA. (inset: i_p vs $\upsilon^{1/2}$ linear plot for respective electrodes, 'm' is slope).

It is generally expected that conducting polymers like PEDOT-PSS or PANI, owing to their porous and redox-active nature, exhibit electroactive areas greater than the geometric area. However, in our study, the observed electroactive areas for PEDOT-PSS, GO/PEDOT-PSS, Au/GO/PEDOT-PSS, WS_2/PEDOT-PSS, Au/WS_2/PEDOT-PSS, and PANI-PVA are lower than the corresponding geometric area. This can be attributed to several factors. Firstly, the film morphology plays a significant role—drop-casted or electrodeposited films, particularly those with incorporated nanomaterials, tend to be denser and more compact, which limits ion diffusion (diffusion limitations within the porous structure) and reduces the exposure of active sites to the electrolyte. Additionally, not all regions of the composite film may be electrochemically accessible due to agglomeration, poor wettability, or partial passivation of the surface, which further lowers the active area. However, several studies have reported electroactive areas significantly lower than the geometric area for polymeric or composite electrode system [35-37]. Despite this, an increase in electroactive area was observed upon modification, especially with the incorporation of GO, AuNPs into PEDOT-PSS, confirming improvement in electrochemical response and overall performance of the system.

3.5. Conclusion

In this chapter the structural, vibrational and morphological characterization of three different composite materials have been discussed. First system evolves electrochemically synthesized PEDOT PSS and its composite with GO and AuNP. Second system comprises PESOT-PSS prepared by electrochemical route and its composite with WS_2 and AuNP. Third system deals with the electrospun nanofibers of PANI-PVA prepared by facile electrospinning technique.

XRD of the first system showed the presence of characteristics peaks of PEDOT-PSS, GO, Au and ITO, confirming the formation of AuNP decorated GO functionalized PEDOT-PSS over the ITO electrode. XRD of the second system displayed the presence of characteristics peaks of PEDOT-PSS, WS_2, Au and ITO, confirming the formation of AuNP decorated WS_2 functionalized PEDOT-PSS over the ITO electrode. The XRD spectra of nanofiber based system revealed the presence of pure PANI and PVA. FTIR results gave the testimony to the existence of functional moieties and the vibrational modes of the fabricated electrodes. FESEM micrographs of the PEDOT-PSS/GO/Au and PEDOT-PSS/WS_2/Au confirmed the uniform deposition of AuNPs over the polymer composite film. Further, EDX analysis was considered to confirm the presence of PEDOT-PSS, GO, Au and WS_2 for both the PEDOT-PSS based hybrid systems.

The electrochemical studies have been performed for AuNP/GO/PEDOT-PSS and AuNP/WS_2/PEDOT-PSS by employing a three-electrode system comprising of synthesized electrode as working electrode, platinum as counter electrode and Ag/AgCl as reference electrode in presence of PBS as an electrolyte. To understand the electroactive properties and charge transfer kinetics between the electrode and electrolyte interface, the prepared electrodes have been characterized by cyclic voltammetry (CV) and electrochemical impedance spectroscopy (EIS) in a three-electrode setup. Results indicates that the hybrid PEDOT-PSS based electrodes in presence of AuNP provides better charge transfer kinetics as compared to the pristine one. Therefore, the presence of chemically inert AuNP layers over polymer-2D composite provides better charge transport mechanism between the electrode-electrolyte interface and also enhances the conductivity of the system. We modified the electrode substrate by preparing nanostructured surfaces that increase electrochemical properties and also serve as a carrier for the biomolecule

immobilization such as enzymes, antibodies and nucleic acids etc. enabling electrochemical signal transduction and amplification.

FESEM micrographs of PANI-PVA composite system resulted formation of abundance of uniform nanofibers. Moreover, smooth fibrous membrane of PANI-PVA composite electrode is expected to provide enhanced binding sites for biomolecules and may offer better sensitivity and linearity resulting as a good candidate for sensing applications.

The scope of the studies is believed to extend the versatility of the carefully chosen composite nanoelectrodes for detection of various analytes with improved selectivity and specificity. In this regard, application of such electrodes in monitoring and sensing target analytes can be found in subsequent chapters.

3.6. References

[1] Baruah, B., Kumar, A., Umapathy, G. R., and Ojha, S. Enhanced electrocatalytic activity of ion implanted rGO/PEDOT: PSS hybrid nanocomposites towards methanol electro-oxidation in direct methanol fuel cells. *Journal of Electroanalytical Chemistry*, 840:35-51, 2019.

[2] Ganguly, A., Sharma, S., Papakonstantinou, P., and Hamilton, J. Probing the thermal deoxygenation of graphene oxide using high-resolution in situ X-ray-based spectroscopies. *The Journal of Physical Chemistry C*, 115(34):17009-17019, 2011.

[3] Zhang, Q., He, Y., Chen, X., Hu, D., Li, L., Yin, T., and Ji, L. Structure and photocatalytic properties of TiO_2-graphene oxide intercalated composite. *Chinese Science Bulletin*, 56:331-339, 2011.

[4] Henglein, A. Radiolytic preparation of ultrafine colloidal gold particles in aqueous solution: optical spectrum, controlled growth, and some chemical reactions. *Langmuir*, 15(20):6738-6744, 1999.

[5] Mapala, K., and Pattabi, M. Mimosa pudica flower extract mediated green synthesis of gold nanoparticles. *NanoWorld J*, 3(2):44-50, 2017.

[6] Cid, C. P., Spada, E. R., and Sartorelli, M. L. Effect of the cathodic polarization on structural and morphological proprieties of FTO and ITO thin films. *Applied surface science*, 273:603-606, 2013.

[7] Basu, A., Ray, S., Chowdhury, S., Sarkar, A., Mandal, D. P., Bhattacharjee, S., and Kundu, S. Evaluating the antimicrobial, apoptotic, and cancer cell gene delivery properties of protein-capped gold nanoparticles synthesized from the edible mycorrhizal fungus Tricholoma crassum. *Nanoscale research letters*, 13:1-16, 2018.

[8] Li, Y., Fan, C. and Zheng, J. A high-efficiency electrochemical sensor of dopamine based on WS_2 nanosheets decorated with dandelion-like platinum–silver nanoparticles. *Journal of Materials Science: Materials in Electronics*, 33(8):5061-5072, 2022.

[9] Cao, S., Liu, T., Zeng, W., Hussain, S., Peng, X., and Pan, F. Synthesis and characterization of flower-like WS_2 nanospheres via a facile hydrothermal route. *Journal of Materials Science: Materials in Electronics*, 25:4300-4305, 2014.

[10] Zhang, X., Lei, W., Ye, X., Wang, C., Lin, B., Tang, H., and Li, C. A facile synthesis and characterization of graphene-like WS_2 nanosheets. *Materials Letters*, 159:399-402, 2015.

[11] Qin, Z., Zeng, D., Zhang, J., Wu, C., Wen, Y., Shan, B., and Xie, C. Effect of layer number on recovery rate of WS_2 nanosheets for ammonia detection at room temperature. *Applied Surface Science*, 414:244-250, 2017.

[12] Kumar, V., Gupta, R. K., Gundampati, R. K., Singh, D. K., Mohan, S., Hasan, S. H., and Malviya, M. Enhanced electron transfer mediated detection of hydrogen peroxide using a silver nanoparticle–reduced graphene oxide–polyaniline fabricated electrochemical sensor. *RSC advances*, 8(2):619-631, 2018.

[13] Singh, W. I., Sinha, S., Devi, N. A., Nongthombam, S., Laha, S., and Swain, B. P. Investigation of chemical bonding and electronic network of rGO/PANI/PVA electrospun nanofiber. *Polymer Bulletin*, 78:6613-6629, 2021.

[14] Deshmukh, M. A., Kang, B. C., and Ha, T. J. Non-enzymatic electrochemical glucose sensors based on polyaniline/reduced-graphene-oxide nanocomposites functionalized with silver nanoparticles. *Journal of Materials Chemistry C*, 8(15):5112-5123, 2020.

[15] Singhal, A., Kaur, M., Dubey, K. A., Bhardwaj, Y. K., Jain, D., Pillai, C. G. S., & Tyagi, A. K. Polyvinyl alcohol–In 2 O 3 nanocomposite films: synthesis,

characterization and gas sensing properties. *RSC advances*, *2*(18), 7180-7189, 2012.

[16] Kanwat, A. and Jang, J. Enhanced organic photovoltaic properties via structural modifications in PEDOT: PSS due to graphene oxide doping. *Materials Research Bulletin*, 74:346-352, 2016.

[17] Yoo, D., Kim, J., and Kim, J. H. Direct synthesis of highly conductive poly (3, 4-ethylenedioxythiophene): poly (4-styrenesulfonate)(PEDOT: PSS)/graphene composites and their applications in energy harvesting systems. *Nano Research*, 7:717-730, 2014.

[18] Kumar, S. S., Kumar, C. S., Mathiyarasu, J., and Phani, K. L. Stabilized gold nanoparticles by reduction using 3, 4-ethylenedioxythiophene-polystyrenesulfonate in aqueous solutions: nanocomposite formation, stability, and application in catalysis. *Langmuir*, 23(6):3401-3408, 2007.

[19] Medhi, A., Baruah, S., Singh, J., Betty, C. A., and Mohanta, D. Au nanoparticle modified GO/PEDOT-PSS based immunosensor probes for sensitive and selective detection of serum immunoglobulin g (IgG). *Applied Surface Science*, 575:151775, 2022.

[20] Kumar, S., Baruah, B., and Kumar, A. Tunable degree of oxidation through variation of H_2O_2 concentration and its effect on structural, optical and supercapacitive properties of graphene oxide powders synthesized using improved method. *Materials Today Communications*, 13:26-35, 2017.

[21] Verma, S., and Dutta, R. K. A facile method of synthesizing ammonia modified graphene oxide for efficient removal of uranyl ions from aqueous medium. *RSC advances*, 5(94):77192-77203, 2015.

[22] Zwarich, R., Smolarek, J., and Goodman, L. Assignment of out-of-plane vibrational modes in benzaldehyde. *Journal of Molecular Spectroscopy*, 38(2):336-357, 1971.

[23] Baruah, B., and Kumar, A. Electrocatalytic acitivity of RGO/PEDOT: PSS nanocomposite towards methanol oxidation in alkaline media. *Electroanalysis*, 30(9):2131-2144, 2018.

[24] Bashir, S., Hina, M., Iqbal, J., Jafer, R., Ramesh, S., and Ramesh, K. Self-healable poly (N, N-dimethylacrylamide)/poly (3, 4-ethylenedioxythiophene)

polystyrene sulfonate composite hydrogel electrolytes for aqueous supercapacitors. *Journal of Energy Storage*, 45:103760, 2022.

[25] Shah, M. S. A. S., Muhammad, S., Park, J. H., Yoon, W. S., and Yoo, P. J. Incorporation of PEDOT: PSS into SnO_2/reduced graphene oxide nanocomposite anodes for lithium-ion batteries to achieve ultra-high capacity and cyclic stability. *RSC Advances*, 5(18):13964-13971, 2015.

[26] Vattikuti, S. P., Byon, C., and Chitturi, V. Selective hydrothermally synthesis of hexagonal WS2 platelets and their photocatalytic performance under visible light irradiation. *Superlattices and Microstructures*, 94:39-50, 2016.

[27] Liang, A., Zhu, D., Xu, L., Zhou, W., Xu, J., and Duan, X. Fabrication of flexible PVA/polyaniline/WS2 composite film and its high capacitance behaviors. *International Journal of Electrochemical Science*, 15(10):10541-10549, 2020.

[28] Khataee, A., Eghbali, P., Irani-Nezhad, M. H., and Hassani, A. Sonochemical synthesis of WS2 nanosheets and its application in sonocatalytic removal of organic dyes from water solution. *Ultrasonics Sonochemistry*, 48:329-339, 2018.

[29] Feng, X., Mao, C., Yang, G., Hou, W., and Zhu, J. J. Polyaniline/Au composite hollow spheres: synthesis, characterization, and application to the detection of dopamine. *Langmuir*, 22(9):4384-4389, 2006.

[30] Jin, Y., Fang, M., & Jia, M. In situ one-pot synthesis of graphene–polyaniline nanofiber composite for high-performance electrochemical capacitors. *Applied surface science*, 308:333-340, 2014.

[31] Subrahmanyama, A. R., Geethaa, V., Alakanandanac, A., and Kumard, J. S. Mechanical and electrical conductivity studies of PANI-PVA and PANI-PEO blends. *International Journal of Material Science*, 2(1):27-30, 2012.

[32] Dutta, P., Biswas, S., Ghosh, M., De, S. K., and Chatterjee, S. The dc and ac conductivity of polyaniline–polyvinyl alcohol blends. *Synthetic metals*, 122(2):455-461, 2001.

[33] Anju, V. P., Jithesh, P. R., and Narayanankutty, S. K. A novel humidity and ammonia sensor based on nanofibers/polyaniline/polyvinyl alcohol. *Sensors and Actuators A: Physical*, 285:35-44, 2019.

[34] Dutta, P., Biswas, S., Ghosh, M., De, S. K., and Chatterjee, S. The dc and ac conductivity of polyaniline–polyvinyl alcohol blends. *Synthetic metals*, 122(2)1:455-461, 2001.

[35] Medhi, A., and Mohanta, D. Development of highly sensitive electrochemical immunosensor using PPy-MoS_2-based nanocomposites modified with 90 MeV C6+ ion beams. *Microchimica Acta*, 191(3):166, 2024.

[36] Tan, H. L., Sanira Putri, M. K., Idris, S. S., Hartikainen, N., Abu Bakar, N. F., Keirouz, A., and Radacsi, N. High-throughput fabrication of carbonized electrospun polyacrylonitrile/poly (acrylic acid) nanofibers with additives for enhanced electrochemical sensing. Journal of Applied Polymer Science, 137(43):49341, 2020.

[37] *Sisolakova, I., Gorejova, R., Chovancova, F., Shepa, J., Ngwabebhoh, F. A., Fedorkova, A. S., ... and Orinakova, R. Polymer-based electrochemical sensor: Fast, accurate, and simple insulin diagnostics tool. Electrocatalysis, 14(5):697-707, 2023.*